New Design Approach for Grid-Current-Based Active Damping of LCL Filter Resonance in Grid-Connected Converters

Mahmoud A. Gaafar[†], Gamal M. Dousoky[*], Emad M. Ahmed[**,***],
Masahito Shoyama[****], and Mohamed Orabi[‡]

[†,‡]APEARC, Faculty of Engineering, Aswan University, Aswan, Egypt
[*]Electrical Engineering Dept., Minia University, Alminia, Egypt
[**]Dept. of Electrical Engineering, Jouf University, Aljouf, Saudi Arabia
[***]Dept. of Electrical Engineering, Faculty of Engineering, Aswan University, Aswan, Egypt
[****]Graduate School of Information Science and Electrical Engineering, Kyushu University, Fukuoka, Japan

Abstract

This paper investigates the active damping of grid-connected LCL filter resonance using high-pass filter (HPF) of the grid current. An expression for such HPF is derived in terms of the filter components. This expression facilitates a general study of the actively damped filter behavior in the discrete time domain. Limits for the HPF parameters are derived to avoid the excitation of unstable open loop poles since such excitation can reduce both the damping performance and the system robustness. Based on this study, straightforward co-design steps for the active damping loop along with the fundamental current regulator are proposed. A numerical example along with simulation and experimental results are presented to verify the theoretical analyses.

Key words: Active damping, Grid, *LCL* filter, Resonance

I. INTRODUCTION

For grid-connected converters, *LCL* filters are more interesting when compared to *L* filters due to their higher attenuation for switching harmonics along with lower weight and volume [1], [2]. From the control view point, the current control strategies developed for grid-connected converters should fulfill a number of objectives include sinusoidal grid current, fast transient response, high robustness against parameters variations, implementation simplicity and achieving zero steady-state error in the grid current [3]. *LCL* filters introduce two extra poles which reduce system stability.

Therefore, achieving the aforementioned objectives for an *LCL* filter based system requires a complex control algorithm equipped with a resonance damping technique [3]. Various linear and non-linear control strategies have been proposed for *LCL* filter based single-phase grid-connected converters.

Hysteresis current control methods can achieve most of the aforementioned objectives such as fast transient response, high robustness to parameter variations and implementation simplicity [4]-[7]. However, keeping the measured current within a hysteresis band results in a variable switching frequency that may result in undesired current harmonics. Sliding mode control based methods offer simple implementation, fast dynamic response and high robustness [8], [9]. However, they suffer from the chattering phenomenon and variable switching frequency. Composite nonlinear feedback and Lyapunov-function based control methods have been adopted. However, their implementation is not simple [10], [11].

Other control methods, such as repetitive control [12], predictive control [13], intelligent control [14] and neural-

network based control [15], have been adopted for the current loop control of inverters. However, there are some limitations associated with these methods. For example, predictive control needs precise system parameters to reach the desired performance, intelligent control has a variable switching frequency that may result in undesired current harmonics, repetitive control shows a slow dynamic response, and neural-network based control requires a complex training process.

Using a conventional PI-based controller in the stationary reference frame results in a steady state error in tracking sinusoidal references [16]. On the other hand, an imaginary control circuit is required if synchronous reference frame implementation is adopted. To overcome the problems of conventional PI controllers in the stationary reference frame, a PR controller has been proposed. PR controllers are widely used in the control of single-phase inverters [11], [17], [18].

From the stability viewpoint, a single grid current control loop can be adopted for resonant frequencies of more than one-sixth of the sampling frequency [1]. However, this technique is not always suitable especially in weak grids where the grid inductance varies significantly. Optimized loop shaping for both a current controller and an active damper (AD) has been proposed in [19] using a complicated fifth-order feedback. Passive damping configurations have been presented in [1][1]. However, they increase both the power losses and the filter size. Recently, active damping by modifying the control system has been getting a lot of attention. A cascade digital filter can be used for this purpose [20]. However, this decreases the system bandwidth and is highly dependent on the varied grid side inductance. Active damping based on state variables feedback is more desirable. In this regard, using the filter capacitor current or voltage feedback have been investigated [21]-[31]. However, these methods make additional current/voltage sensors or complicated estimation loops necessary.

Grid-current-based active damping is more desirable since there is no need for additional sensors or complicated control algorithms. Ideally, this needs an s^2 term in the active damping loop [32]. However, it is not implemented practically due to noise amplification. Two approaches have been presented in the literature to overcome this issue. One of these approaches employs a second order Infinite Impulse Response (IIR) filter [33]. However, the control system is complicated and a large number of iterations are needed to meet pre-specified behavior. The second approach, which is the main focus of this paper, employs a HPF of the grid current feedback [32], [34]-[36]. In [32], a HPF is designed in the s-domain to behave as an ideal s^2 term around the resonant frequency. However, these studies do not provide straightforward design steps especially for discrete implementation. In [34], an independent design for an HPF and Synchronous Rotating Frame Proportional-Integrator

(SRFPI) current regulator has been proposed.

In both [16] and [18], there is no consideration of the transport delays of the digitally controlled systems and their effect on the open loop system stability which, upon violation, can decline the damping performance and the system robustness. Moreover, as indicated in [35], both the AD and the fundamental current regulator must be designed together to achieve a pre-specified performance.

Based on s-domain emulation of a digitally controlled system, a virtual impedance model for a grid-current-based actively damped filter has been derived in [35] as a shunt impedance across the grid side inductance. It was determined that unstable open loop behavior can be avoided for resonant frequencies up to 0.28 of the sampling frequency. However, for certain resonant frequencies, it cannot identify the parametric influence of the HPF on the open loop stability. Consequently, the tuning process becomes tedious and a lot of iterations are needed to design the HPF along with the fundamental current regulator without open loop stability violation. In addition, it is cost effective to design LCL filters with higher resonant frequencies, and without violation of open loop stability especially when selective harmonic compensation is of concern [25].

From the above discussion, the following challenges can be identified when handling grid-current-based active damping.

- Extending the resonant frequency range over which unstable open loop behavior can be avoided.
- Identifying the parametric influence of the HPF on the open loop system stability of digitally controlled systems.
- Straightforward design steps for the HPF along with the fundamental current regulator.

Following this introduction, an expression of the HPF is derived. Using this expression, a detailed study for the actively damped filter is carried out in the discrete time domain to clarify the effect of HPF parameters on open loop stability. After that, straightforward design steps for the HPF along with the fundamental current regulator are presented. To verify the theoretical analyses, a numerical example along with experimental results at different resonant frequencies are presented. Finally, some conclusions are introduced.

II. PROPOSED HPF FORM FOR ACTIVE DAMPING

A. System Description

Using an LCL filter, a grid-connected single phase inverter is shown in Fig. 1. The control system is shown in Fig. 2. A proportional resonant (PR) controller, represented in (1) as $G_c(s)$, is used as a current regulator with $\omega_o = 2\pi f_o$, where ω_o and f_o are the grid frequency in rad/sec and Hz, respectively. Proportional capacitor current feedback (H_d) is adopted as the AD for the filter resonance. The filter resonant frequency is expressed in (2) in rad/sec.
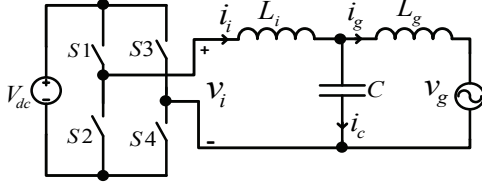
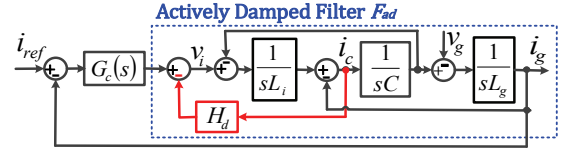Fig. 1. Inverter connected to a grid through an *LCL* filter.

Fig. 2. System block diagram with capacitor current feedback.
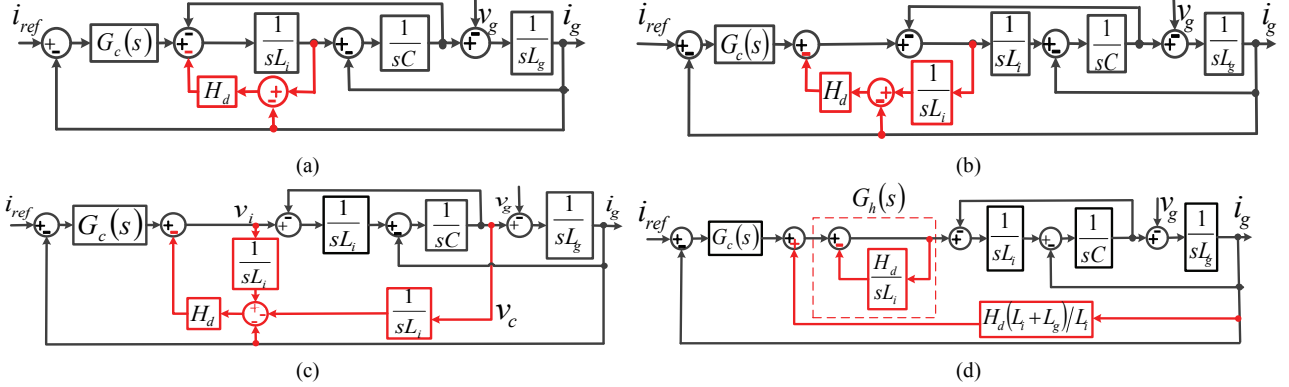

(a)

(b)

(c)

(d)

Fig. 3. Manipulation of the active damping method, which uses a proportional feedback of the capacitor current, sequentially from (a) to (d).

$$G_c(s) = K_p + \frac{K_r s}{s^2 + \omega_o^2} \qquad (1)$$

$$\omega_{res} = \sqrt{(L_i + L_g)/(C L_i L_g)} \qquad (2)$$

This system is manipulated in Fig. 3. From Fig. 3(c), the capacitor current feedback is equivalent to three feedback loops of the modulated inverter voltage (v_i), the capacitor voltage (v_c) and the grid current (i_g). The system is further manipulated in Fig. 3(d) as follows.

- The capacitor voltage feedback is shifted towards the grid current producing a proportional term $(H_d(L_i + L_g)/L_i)$.
- The modulated voltage feedback is augmented as a cascaded HPF and expressed as $G_h(s)$ in (3) where $\omega_h = H_d/L_i$.

$$G_h(s) = \frac{1}{\omega_h} \cdot \frac{s}{1 + s/\omega_h} \qquad (3)$$

B. Proposed Active Damper Expression

The HPF $G_h(s)$ in Fig. 3(d) is eliminated from the main control loop and inserted in the grid current damping loop as shown in Fig. 4. The damping feedback loop is still a HPF, expressed in (4) as $G_{ad}(s)$. To acquire flexibility, the gain of $G_{ad}(s)$ is re-written in (5) as the product of a new variable (r) with a constant quantity ($L_i + L_g$).

$$G_{ad}(s) = \frac{s(L_i + L_g)}{1 + s/\omega_h} \qquad (4)$$

$$G_{ad}(s) = \frac{sr(L_i + L_g)}{1 + s/\omega_h} \qquad (5)$$

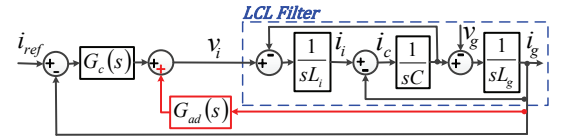Unlike the general HPF expressions used in [32],[34]-[35],

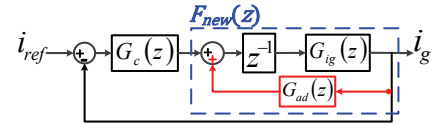Fig. 4. System block diagram with a HPF of the grid current feedback.

Fig. 5. Discrete representation of the overall system.

expressing the HPF gain in terms of the filter inductances helps clarify the parametric influence of the HPF on open loop stability as indicated in the following sections.

III. DISCRETE IMPLEMENTATION

A. System Discretization

Fig. 5 shows the system discrete representation where $G_{ig}(z)$ is the discrete transfer function relating the modulated inverter voltage to the grid current. It is determined using a zero-order-hold (ZOH) discretization of its continuous counterpart $G_{ig}(s)$. Both $G_{ig}(s)$ and $G_{ig}(z)$ are expressed in (6) and (7), respectively. $G_c(s)$ and $G_{ad}(s)$ are discretized using Tustin approximations as expressed in (8) and (9) where T_s denotes the sampling time. The digital signal processor (DSP) delay is modeled by one sample delay.

$$G_{ig}(s) = \frac{I_g(s)}{V_i(s)} = \frac{1}{L_i L_g C s (s^2 + \omega_{res}^2)} \qquad (6)$$
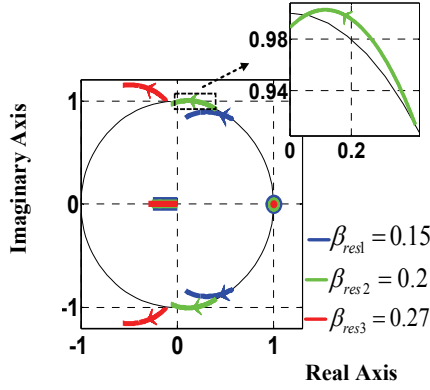
Fig. 6. Pole maps of $F_{new}(z)$ with sweeping β_h (at $r=1$ and different β_{res}).
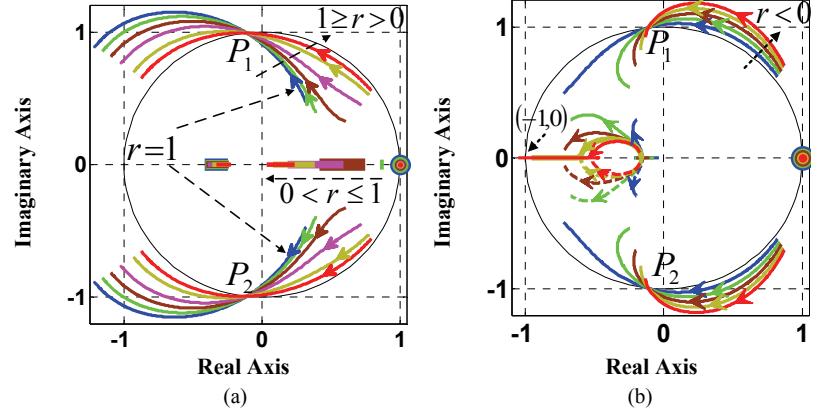
Fig. 7. Pole maps of $F_{new}(z)$ with sweeping β_{res} at $\beta_h=0.5$ and different values of r: (a) $1 \geq r > 0$; (b) $r < 0$.

$$G_{ig}(z) = \frac{T_s}{(L_i+L_g)}\left(\frac{(1-\alpha)z^2-2(cos(\delta)-\alpha)z+(1-\alpha)}{(z-1)(z^2-2z\,cos(\delta)+1)}\right) \quad (7)$$

$$G_c(z) = K_p + K_r \frac{sin(\omega_o T_s)}{2\omega_o}\frac{z^2-1}{(z^2-2z\,cos(\omega_o T_s)+1)} \quad (8)$$

$$G_{ad}(z) = K_{ad}\frac{z-1}{z+\omega_{ad}} \quad (9)$$

where:

$$\delta = \omega_{res}T_s, \qquad \alpha = \frac{sin(\omega_{res}T_s)}{\omega_{res}T_s},$$

$$K_{ad} = \frac{2\omega_h r(L_i+L_g)}{\omega_h T_s+2}, \qquad \omega_{ad} = \frac{\omega_h T_s-2}{\omega_h T_s+2} \quad (10)$$

To generalize the analyses, both ω_{res} and ω_h are expressed in terms of the sampling frequency (ω_s) as in (11). Then the expressions in (10) are re-written in (12).

$$\omega_{res} = \beta_{res}\omega_s, \qquad \omega_h = \beta_h\omega_s \quad (11)$$

$$\delta = 2\pi\beta_{res}, \qquad \alpha = \frac{sin(2\pi\beta_{res})}{2\pi\beta_{res}},$$

$$K_{ad} = \frac{2\omega_h r(L_i+L_g)}{2\pi\beta_h+2}, \qquad \omega_{ad} = \frac{2\pi\beta_h-2}{2\pi\beta_h+2} \quad (12)$$

Using (7), (9) and (12), the actively damped filter ($F_{new}(z)$) is expressed in (13). Its gain depends on the specific values of the sampling frequency and the filter inductances. However, the zeros and poles of $F_{new}(z)$ do not depend on these specific values. They depend on r (the gain-multiplier of the HPF), β_{res} (the ratio of ω_{res} to ω_s) and β_h (the ratio of ω_h to ω_s). Since the PR controller expressed in (8) does not have any unstable poles, the open loop stability ($T_{open}(z) = G_c(z)F_{new}(z)$) is implied only by $F_{new}(z)$, and in turn, by r, β_{res} and β_h.

In the next sections, the effects of r, β_{res} and β_h on the stability of $F_{new}(z)$ are investigated. From (13), $F_{new}(z)$ has one constant pole at $z=1$ and four poles that depend on r, β_{res} and β_h; two resonant poles, and other two are called non-resonant poles.

B. Discussing the Effects of the HPF Parameters

In Fig. 6, the pole map of $F_{new}(z)$ is plotted by sweeping β_h from 0 to 0.5 (corresponding to ω_h, which is equal to the Nyquist frequency) at a constant value of $r=1$ (corresponding to a HPF gain of (L_i+L_g)) and three values of β_{res} ($\beta_{res1}<\beta_{res2}<\beta_{res3}$; corresponding to different resonant frequencies). The following remarks can be revealed from this plot.

1. In addition to the constant pole at $z=1$, one of the non-resonant poles is also constant at $z=1$. The second non-resonant pole tracks entirely inside the unit circle for all values of β_{res} (its track direction is not shown for the sake of clarity).

2. The tracks of the resonant poles start from some point on the unit circle (corresponding to an undamped LCL filter). By increasing β_h, the resonant poles can track entirely inside the unit circle (as for β_{res1}), or they can track entirely outside the unit circle (as for β_{res3}). In addition, they can initially track outside the unit circle before tracking inside the unit circle above a certain value of β_h (as for β_{res2}).

From the second remark, it is expected that there is a maximum limit for β_{res} above which $F_{new}(z)$ is unstable in the range of β_h (<0.5). This maximum limit is denoted as $\beta_{res-max}$ (corresponding to the resonant frequency of $\omega_{res-max}$). At $\beta_{res-max}$, the resonant poles should track outside the unit circle and end by an intersection with the unit circle at $\beta_h=0.5$. Based on this understanding, $\beta_{res-max}$ is determined by plotting a pole map of $F_{new}(z)$ while sweeping β_{res} at a constant value of $\beta_h=0.5$.

To investigate the effect of HPF gain variations, pole maps are plotted for the two regions of ($0<r\leq1$) and ($r<0$) as shown in Figs. 7 (a) and (b), respectively. In these plots, β_{res} is swept from 0.1 to 0.45 (theoretically, β_{res} can be extended to 0.5. However, due to resonant frequency variations with discrete implementation, the resonant frequency should be adequately far from the vicinity of the Nyquist frequency [37]). From
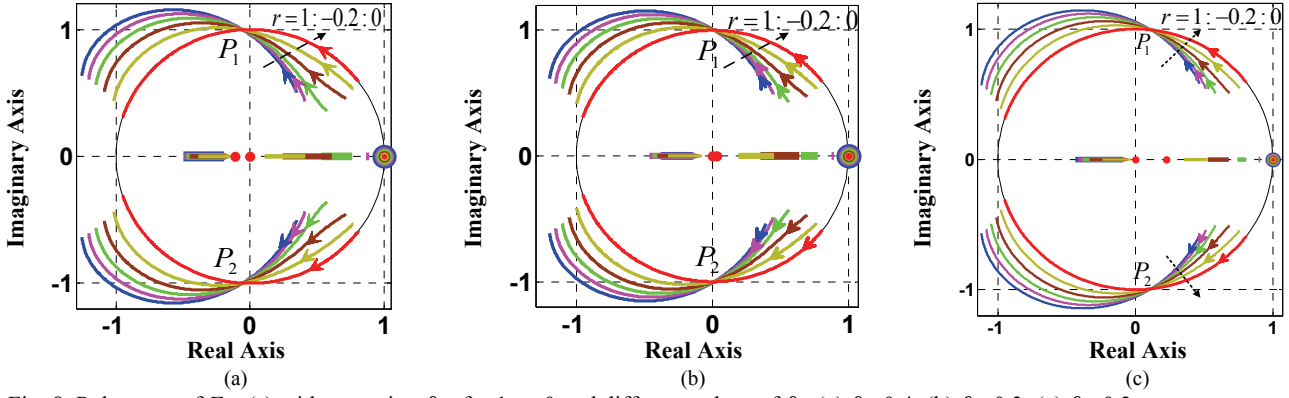
Fig. 8. Pole maps of $F_{new}(z)$ with sweeping β_{res} for $1 \geq r > 0$ and different values of β_h: (a) $\beta_h = 0.4$; (b) $\beta_h = 0.3$; (c) $\beta_h = 0.2$.
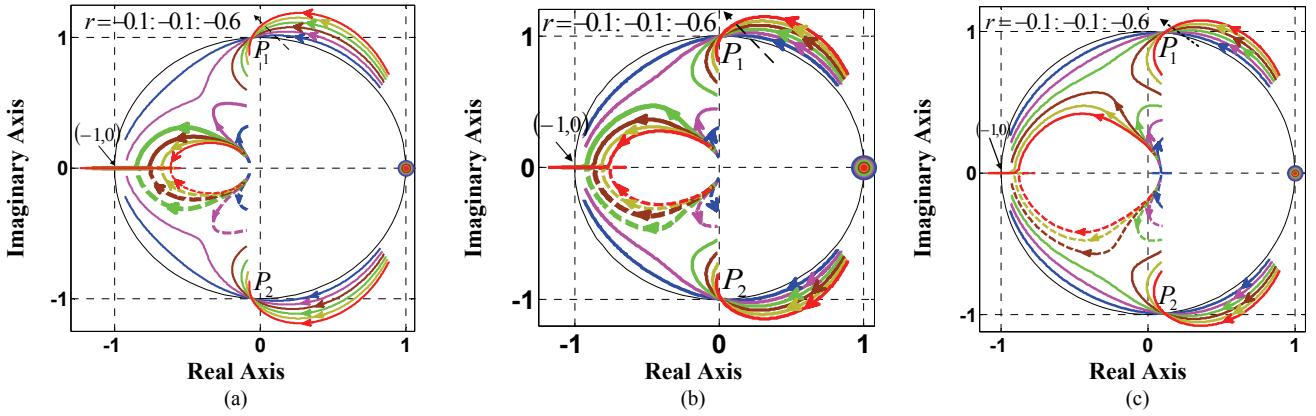

Fig. 9. Pole maps of $F_{new}(z)$ with sweeping β_{res} for $r < 0$ at different values of β_h: (a) $\beta_h = 0.4$; (b) $\beta_h = 0.3$; (c) $\beta_h = 0.2$.

these figures, it can be revealed that:

- *For $0 < r \leq 1$:* in Fig. 7(a), the resonant poles track initially inside the unit circle before tracking outside the unit circle above a certain value of $\beta_{res} = \beta_{res-max}$. It is observed that all of the tracks of the resonant poles intersect with the unit circle at certain points corresponding to the resonant poles denoted as $P_{1,2}$. Accordingly, for $0 < r \leq 1$, $F_{new}(z)$ is stable only for resonant frequencies below the value of $\omega_{res-max} (= \beta_{res-max} \omega_s)$.

- *For $r < 0$:* in Fig. 7(b), the resonant poles track initially outside the unit circle before tracking inside the unite circle above a certain value of β_{res}. This value is denoted as $\beta_{res-min}$. Furthermore, it is observed that all of the tracks of the resonant poles intersect with the unit circle at the points corresponding to the resonant poles $P_{1,2}$. For the low values of r in this region and with increasing β_{res} above $\beta_{res-min}$, one of the non-resonant poles tracks outside the unit circle above ~~a~~ certain value of β_{res} corresponding to one of the non-resonant poles at (-1,0). This value is denoted as $\beta_{res-high}$. Accordingly, for a certain value of $r < 0$, $F_{new}(z)$ is stable only over the resonant frequency range between $\omega_{res-min} (= \beta_{res-min} \omega_s)$ and $\omega_{res-high} (= \beta_{res-high} \omega_s)$. By decreasing r in this region, the range between $\beta_{res-min}$ and $\beta_{res-high}$ shrinks untill it vanishes at a certain r corresponding to $\beta_{res-min} = \beta_{res-high}$.

This value of r is denoted as r_b with the corresponding β_{res} denoted as β_{res-b}.

C. HPF Cutoff Frequency Variations at Different HPF Gains

For the two regions of r ($0 < r \leq 1$ and $r < 0$), the above analyses are repeated in Figs. 8 and 9 for three values of β_h (0.4, 0.3 and 0.2). It is shown that by decreasing β_h, the resonant poles $P_{1,2}$ move to the right on the unit circle. The performance in the two ranges of r is still the same. For $0 < r \leq 1$, $F_{new}(z)$ is stable below a certain value of $\beta_{res} = \beta_{res-max}$; for $r < 0$, $F_{new}(z)$ is stable over a certain range of $\beta_{res-min} < \beta_{res} < \beta_{res-high}$.

IV. REGIONS FOR A STABLE OPEN LOOP SYSTEM

Two regions of r can be identified for a certain β_h as follows:

1. $0 < r \leq 1$; for a certain r in this region, $F_{new}(z)$ is stable only for resonant frequencies below a certain value of $\omega_{res-max}$.

2. $0 > r \geq r_b$; for a certain r in this region, $F_{new}(z)$ is stable only over the resonant frequency range of $\omega_{res-min} < \omega_{res} < \omega_{res-high}$.

The values of $\beta_{res-max}$, $\beta_{res-min}$, β_{res-b} and r_b can be determined for a certain value of β_h as follows. At $\beta_{res-max}$ or $\beta_{res-min}$, it was
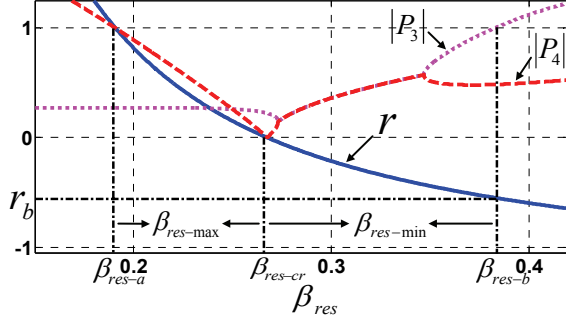
Fig. 10. HPF gain factor (r) along with $|P_3|$ and $|P_4|$ versus $\beta_{res-max}/\beta_{res-min}$ at $\beta_h=0.5$.

shown that $F_{new}(z)$ has five poles: one pole at $z=1$, two resonant poles at $P_{1,2}$ and two non-resonant poles (denoted as P_3 and P_4). Accordingly, the denominator of $F_{new}(z)$ at $\beta_{res-max}$ or $\beta_{res-min}$ can be expressed as (14).

$$den\big(F_{new}(z)\big)\big|_{\beta_{res-max}/\beta_{res-min}} =$$
$$(z-1)(z \pm P_{1,2})(z - P_3)(z - P_4) \qquad (14)$$

By expanding (14) and equating its coefficients with the denominator coefficients of $F_{new}(z)$, expressed in (13), the expressions of (15), (16) and (17) are derived to determined r, P_3 and P_4, respectively.

$$r = \frac{2\pi\beta_h+2}{4\pi\beta_h} \cdot \frac{\cos\delta - Real\{P_{1,2}\}}{(1-\alpha) \cdot Real\{P_{1,2}\}+\alpha-\cos\delta} \qquad (15)$$

$$P_3 =$$
$$\frac{1}{2}\Bigg(2\cos\delta - \omega_{ad} - 2Real\{P_{1,2}\} -$$
$$\sqrt{\big(2\cos\delta - \omega_{ad} - 2Real\{P_{1,2}\}\big)^2 + \frac{16r\pi\beta_h(1-\alpha)}{2\pi\beta_h+2}}\Bigg) \qquad (16)$$

$$P_4 = \frac{4r\pi\beta_h(1-\alpha)}{(2\pi\beta_h+2)P_3} \qquad (17)$$

At a β_h of 0.5, Fig. 10 plots r and the magnitudes of P_3 and P_4 versus $\beta_{res-max}/\beta_{res-min}$. Using this figure, it can be implied that:

a. For $0<r\le1$, the minimum limit of $\beta_{res-max}$ corresponds to $r=1$ and is denoted as β_{res-a}. With a decreasing r, $\beta_{res-max}$ increases untill reaches its maximum limit at $r=0$. On the other hand, for $0>r\ge r_b$, the maximum limit of $\beta_{res-min}$ corresponds to $r_{min} = r_b$. With an increasing r, $\beta_{res-min}$ decreases till it reaches its minimum limit at $r=0$. At $r=0$, both $\beta_{res-max}$ and $\beta_{res-min}$ have the same value which is denoted as β_{res-cr} and expressed in (18) by substituting $r=0$ into (15). It is shown from Figs. 8 and 9 that decreasing β_h causes a movement to the right for the poles $P_{1,2}$ on the unit circle. This in turn increases $real\{P_{1,2}\}$. Accordingly, from (18), β_{res-cr} decrease as β_h

decreases. Then the maximum value of β_{res-cr} corresponds to $\beta_h=0.5$, where $real\{P_{1,2}\}$ is determined from Figs. 7(a) or 7(b) as -0.111. By substituting this value into (18), the maximum value of β_{res-cr} is determined as 0.268. Therefore, for $0<r\le1$, $F_{new}(z)$ can only be stable for resonant frequencies less than $0.268\omega_s$.

$$\beta_{res-cr} = \frac{\cos^{-1}(Real\{P_{1,2}\})}{2\pi} \qquad (18)$$

b. For $0>r\ge r_b$, both r_b and β_{res-b} correspond to one pole of P_3 or P_4 at (-1,0). Thus, r_b and β_{res-b} can be determined from Fig. 10 by locating their values at the unity magnitudes of P_3 or P_4. $\beta_{res-high}$ does not correspond to the resonant poles at $P_{1,2}$. It only corresponds to one pole of P_3 or P_4 at (-1,0). Therefore, it cannot be determined from Fig. 10. However, at high values of r in its second region, the non-resonant poles track entirely inside the unit circle over the entire range of β_{res} as shown in Fig. 9 (e.g. the non-resonant poles track entirely inside the unit circle for r of -0.1 and -0.2). Hence, the stable range of $F_{new}(z)$ can be extended to a $\beta_{res-high}$ of 0.45 (the maximum considered limit of β_{res}) using high values of r in its second region.

Using Fig. 10, at a constant β_h, the stable regions of $F_{new}(z)$ can be re-identified depending on β_{res} as follows:

1. For $\beta_{res} \le \beta_{res-a}$, $F_{new}(z)$ can only be stable in the first region of r ($0<r\le1$).
2. For $\beta_{res-a}<\beta_{res}<\beta_{res-cr}$, $F_{new}(z)$ can only be stable over a certain range in the first region of r between 0 and the value of r corresponding to β_{res} in Fig. 10.
3. For $\beta_{res-cr}<\beta_{res}<\beta_{res-b}$, $F_{new}(z)$ can only be stable over a certain range in the second region of r between 0 and the value of r corresponding to β_{res} in Fig. 10.

V. CONTROL SYSTEM DESIGN

A. HPF Cutoff Frequency Tuning (β_h tuning)

To tune β_h, pole maps of $F_{new}(z)$ are plotted with sweeping β_h for different values of β_{res} in two identified regions of r:

- First region; $0<r\le1$, pole maps are plotted in Figs. 11(a), (b) and (c) for three values of r at 0.2, 0.5 and 0.8, respectively. In each figure, three β_{res} values of 0.17, 0.2 and 0.24 are considered (these values are less than $\beta_{res-cr}=0.268$ since above this value, a positive r cannot be used for the stability of $F_{new}(z)$). By increasing β_h, the resonant poles may track entirely outside or inside the unit circle or they may initially track outside the unit circle before tracking inside the unit circle with an increasing β_h. To ensure the stability of $F_{new}(z)$, high β_h

$$F_{new}(z) = \frac{z^{-1}G_{ig}(z)}{1-z^{-1}G_{ad}(z)G_{ig}(z)} = \frac{T_s}{(L_i+L_g)} \cdot \frac{(z+\omega_{ad})\big((1-\alpha)z^2-2(cos(\delta)-\alpha)z+(1-\alpha)\big)}{(z-1)\Big[z(z+\omega_{ad})(z^2-2z\,cos(\delta)+1)-\frac{4\pi r\beta_h}{2\pi\beta_h+2}\big((1-\alpha)z^2-2(cos(\delta)-\alpha)z+(1-\alpha)\big)\Big]} \qquad (13)$$
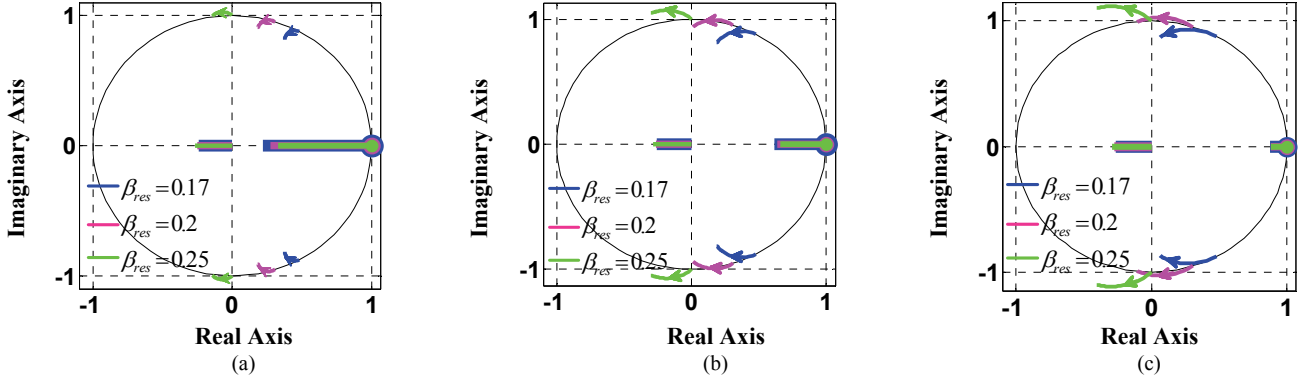
Fig. 11. Pole maps of $F_{new}(z)$ with sweeping β_h at different β_{res} and different values of r in the first region $(0<r\leq1)$: (a) r=0.2; (b) r=0.5; (c) r=0.8.
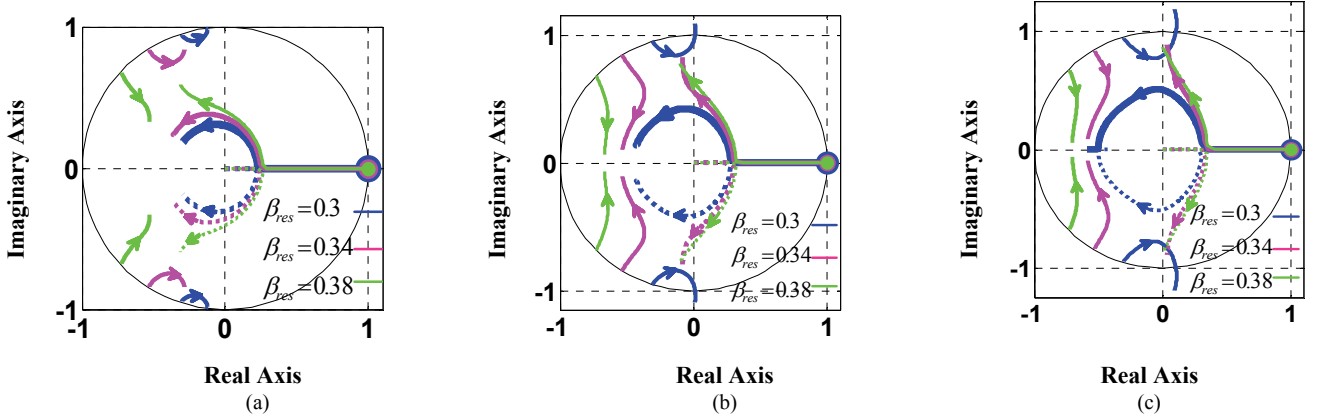

Fig. 12. Pole maps of $F_{new}(z)$ with sweeping β_h at different β_{res} and different values of r in the second region $(0>r\geq r_b)$: (a) r=-0.2; (b) r=-0.4; (c) r=-0.6.
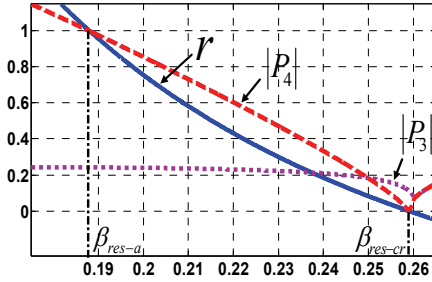

Fig. 13. HPF gain factor (r) along with $|P_3|$ and $|P_4|$ versus $\beta_{res\text{-}max}$ at β_h=0.4.
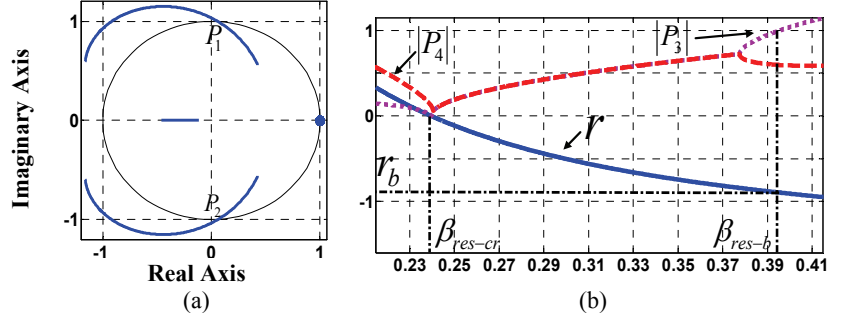
Fig. 14. At β_h=0.25: (a) Pole map of $F_{new}(z)$; (b) HPF gain factor (r) along with $|P_3|$ and $|P_4|$ versus $\beta_{res\text{-}min}$.

should be adopted. Theoretically, β_h can be extended to 0.5. However, such a value can deteriorate the discretization process. A value of β_h=0.4 is adopted. At this value, $\beta_{res\text{-}cr}$ and $\beta_{res\text{-}a}$ are determined by plotting the pole map of $F_{new}(z)$ with sweeping β_{res} at any constant value of r (any of the pole maps in Fig. 8(a) or Fig. 9(a) can be used). From these figures, real$\{P_{1,2}\}$ is determined to be -0.0562. Using (15), (16) and (17), Fig. 13 plots r along with the magnitudes of P_3 and P_4 versus $\beta_{res\text{-}max}/\beta_{res\text{-}min}$ in the first region of r. From this figure, $\beta_{res\text{-}a}$ and $\beta_{res\text{-}cr}$ are determined to be 0.188 and 0.259, respectively. Then the first and the second regions of β_{res}

at β_h=0.4 are identified since $\beta_{res} \leq 0.188$ and $0.188<\beta_{res}<0.259$, respectively.

- *Second region*; $0>r\geq r_b$, pole maps of $F_{new}(z)$ are plotted in Figs. 12 (a), (b) and (c) for values of r at -0.2, -0.4 and -0.6, respectively. Three β_{res} values of 0.3, 0.34 and 0.38 are considered. By increasing β_h, the resonant poles may track entirely inside the unit circle or they may initially track inside the unit circle before tracking outside the unit circle with an increasing β_h. From these pole maps, using a medium value for $\beta_h (0.25)$ is a good tradeoff to ensure the stability of $F_{new}(z)$. At this value, $\beta_{res\text{-}cr}$ and $\beta_{res\text{-}b}$ can be determined by plotting the pole

map of $F_{new}(z)$ with sweeping β_{res} at any value of r ($r=1$ is used) as shown in Fig. 14(a), where $real\{P_{1,2}\}$ is determined as 0.0653. Using (15), (16) and (17), Fig. 14 (b) plots r and the magnitudes of P_3 and P_4 versus $\beta_{res-max}/\beta_{res-min}$ in the second region of r. From this figure, β_{res-cr} and β_{res-b} are determined as 0.239 and 0.395, respectively. In addition, r_b is determined as -0.875. Then the third region of β_{res} at $\beta_h=0.25$ is identified as $0.239<\beta_{res}<0.395$. Note that, as indicated previously, for values of $0.395<\beta_{res}<0.45$, higher values of r in the second region have to be adopted to stabilize $F_{new}(z)$ (e.g. -0.1 and -0.2).

- If β_{res} is between 0.239 (β_{res-cr} at $\beta_h=0.25$) and 0.259 (β_{res-cr} at $\beta_h=0.4$), a β_h of either 0.25 or 0.4 with the corresponding regions of r can be used.

B. Control Parameters Design

The design objectives for the overall system are:
1. To ensure the stability of $F_{new}(z)$.
2. To meet pre-specified limits of the fundamental loop gain (T_{fo}) and crossover frequency (ω_c).

An s-domain model, shown in Fig. 15, is used to design the control parameters. An exponential function of $G_d(s) = e^{-1.5sT_s}$ is used to model the DSP delay [22]. The PR controller ($G_c(s)$) is expressed here by its proportional gain (K_p) for frequencies higher than ω_o and by its resonant gain (K_r) at ω_o.

Since the crossover frequency should be sufficiently higher than ω_o, and below both ω_{res} and the adopted values of ω_h ($0.25\omega_s$ or $0.4\omega_s$), the loop transfer function (T_{loop}) at ω_c can be approximated using trigonometry as in (19), where A_c and θ_c are expressed in (20). Then the loop gain at ω_c can be expressed as in (21). Then K_p can be determined as in (22).

$$T_{loop}(j\omega_c) = K_p \frac{e^{-j1.5\omega_c T_s}}{j\omega_c(L_i+L_g)(1-re^{-j1.5\omega_c T_s})}$$

$$= K_p \frac{e^{-j1.5\omega_c T_s}}{j\omega_c(L_i+L_g)A_c e^{j\theta_c}} \quad (19)$$

$$A_c = \sqrt{1+r^2-2r\cos(1.5T_s\omega_c)}$$
$$\theta_c = \sin^{-1}\frac{r\sin(1.5\omega_c T_s)}{A} \quad (20)$$

$$\left|T_{loop-d}(j\omega_c)\right| = \frac{K_p}{\omega_c(L_i+L_g)A_c} = 1 \quad (21)$$

$$K_p = \omega_c(L_i+L_g)A_c \quad (22)$$

Similarly, the loop gain at ω_o is approximated in dB in (23). Then K_r can be determined using (24).

$$T_{fo} = 20\log_{10}\frac{K_r}{\omega_o(L_i+L_g)A_o} \quad (23)$$

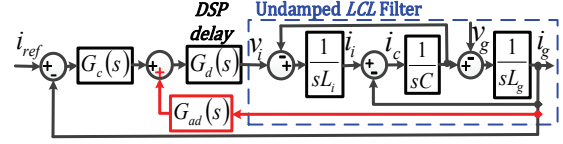$$K_r = \omega_o(L_i+L_g)A_o \cdot 10^{\frac{T_{fo}}{20}} \quad (24)$$
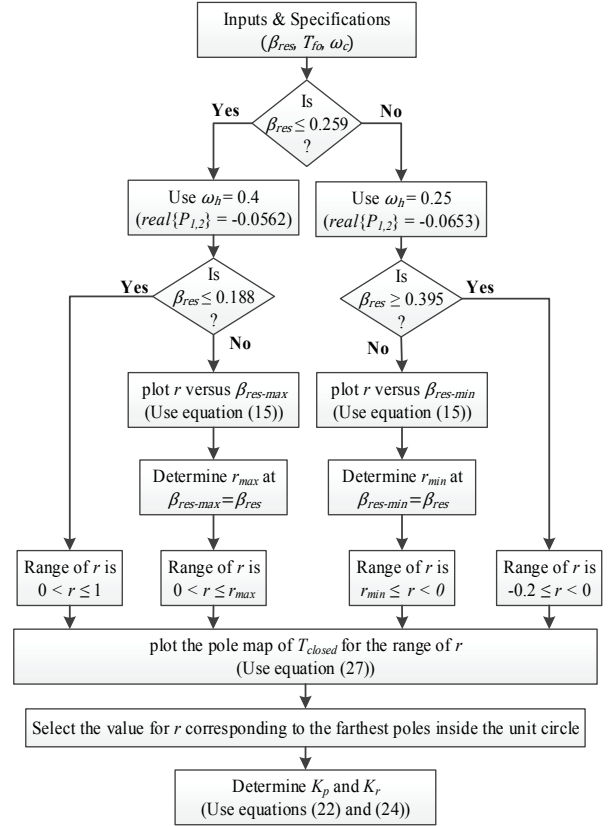

Fig. 15. Equivalent s-domain model.

Fig. 16. Design flow for the control parameters.

where:

$$A_o = \sqrt{1+r^2-2r\cos(1.5T_s\omega_o)} \quad (25)$$

By substituting (22) and (24) into (8), $G_c(z)$ is expressed in terms of r and the pre-specified quantities as in (26).

$$G_c(z) = \omega_c(L_i+L_g)A_c + \frac{\omega_o(L_i+L_g)A_o\cdot 10^{\frac{T_{fo}}{20}}\cdot\sin(\omega_o T_s)(z^2-1)}{2\omega_o(z^2-2z\cos(\omega_o T_s)+1)} \quad (26)$$

From Fig. 5, the discrete closed loop transfer function is expressed in (27).

$$T_{closed}(z) = \frac{G_c(z)F_{new}(z)}{1+G_c(z)F_{new}(z)} \quad (27)$$

Using the above-addressed expressions, Fig. 16 shows the design flow of the control parameters.

VI. NUMERICAL AND EXPERIMENTAL VERIFICATION

A. Numerical Example

Table I presents the parameters of the system shown in
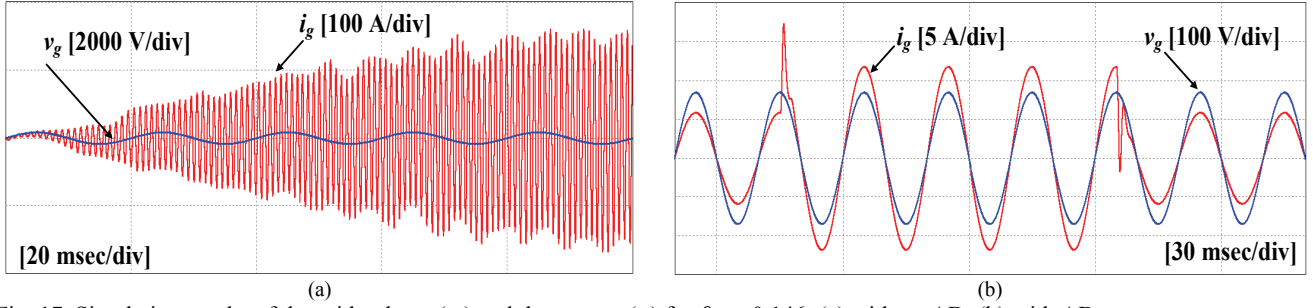
Fig. 17. Simulation results of the grid voltage (v_g) and the current (i_g) for β_{res1}=0.146: (a) without AD; (b) with AD.
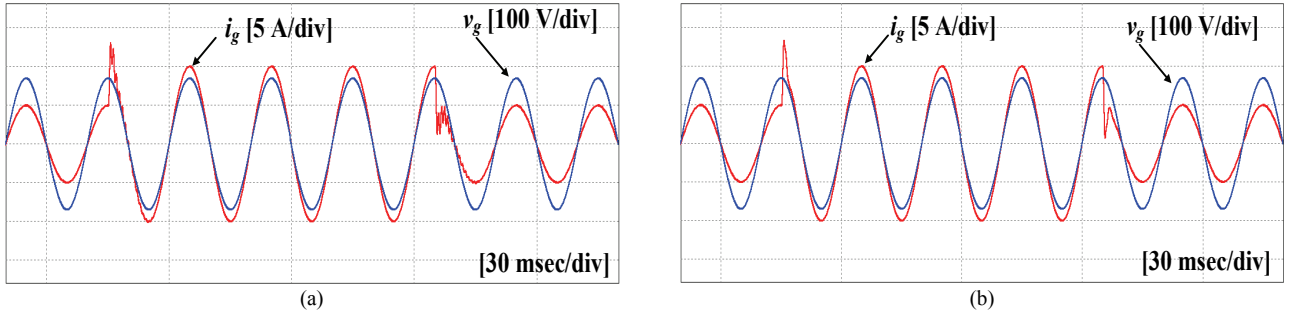
Fig. 18. Simulation results of the grid voltage (v_g) and the current (i_g) for β_{res2}=0.197: (a) without AD; (b) with AD.

Fig. 19. Simulation results of the grid voltage (v_g) and the current (i_g) with AD at: (a) β_{res3}=0.296; (b) β_{res4}=0.379.

Fig. 20. Experimental measurements of the grid voltage (v_g) and the current (i_g) for β_{res1}=0.146: (a) without AD; (b) with AD.

Fig. 21. Experimental measurements of the grid voltage (v_g) and the current (i_g) for β_{res2}=0.197: (a) without AD; (b) with AD.

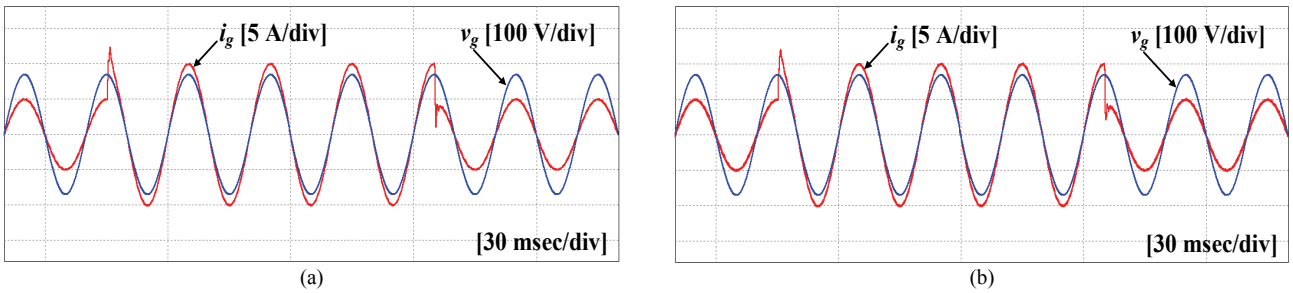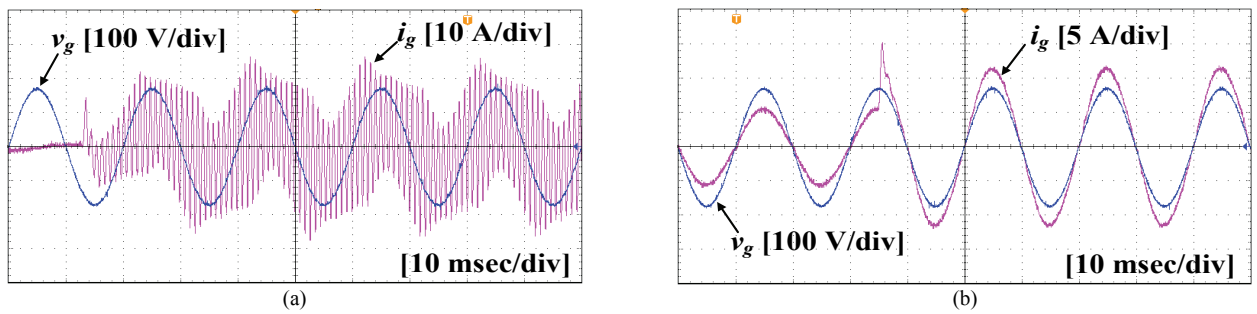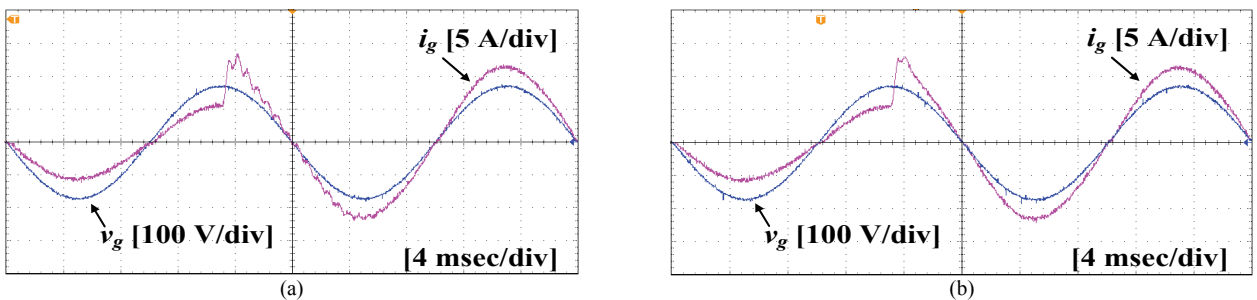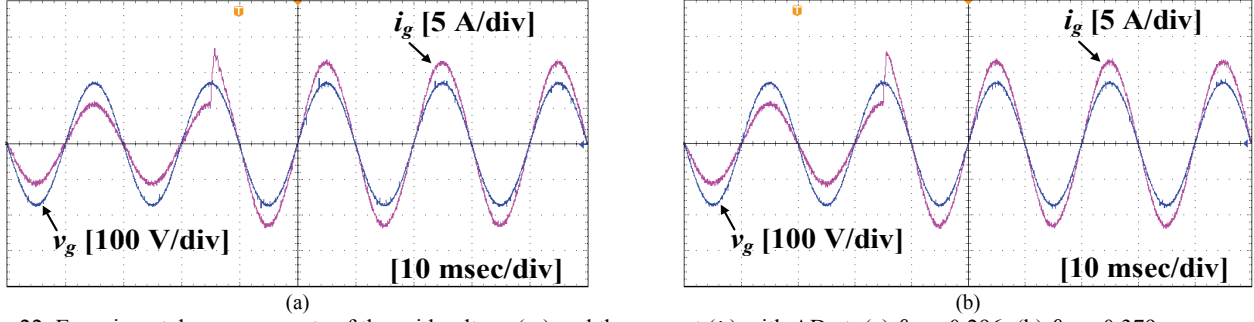Fig. 22. Experimental measurements of the grid voltage (v_g) and the current (i_g) with AD at: (a) β_{res3}=0.296; (b) β_{res4}=0.379.

Fig. 1. The proposed tuning steps are applied to the four values of the resonant frequencies ω_{res1}, ω_{res2}, ω_{res3} and ω_{res4}, corresponding to β_{res} of 0.146 (β_{res1}), 0.197 (β_{res2}), 0.296 (β_{res3}) and 0.379 (β_{res4}), respectively. T_{fo} is specified as 65 dB, and ω_c is specified as the ratio of the corresponding resonant frequency as follows: $0.3\omega_{res1}$, $0.25\omega_{res2}$, $0.22\omega_{res3}$ and $0.18\omega_{res4}$.

At the beginning, a value of β_h=0.4 is adopted for β_{res1} and β_{res2}. On the other hand, a value of β_h=0.25 is adopted for β_{res3} and β_{res4}. Then for these values of β_h, Figs. 13 and 14(b) plot r versus $\beta_{res\text{-}max}/\beta_{res\text{-}min}$. From Fig. 13, r for β_{res2} a determined as 0.83. From Fig. 14 (b), r for β_{res3} and β_{res4} are determined as -0.48 and -0.84, respectively. To complete the tuning process, the pole map of $T_{closed}(z)$ is plotted over the corresponding stable range of r for each value of β_{res} as follows:

- $0<r\leq1$ for β_{res1}=0.146 (<0.188).
- $0<r<0.83$ for β_{res2}=0.197.
- $0>r>-0.48$ for β_{res3}=0.296.
- $0>r>-0.84$ for β_{res4}=0.379.

These pole maps are not shown here. The values of r corresponding to the farthest closed loop poles inside the unit circle are selected as 0.24, 0.16, -0.12 and -0.18 for β_{res1}, β_{res2}, β_{res3} and β_{res4}, respectively. Finally, K_p and K_r are determined from (22) and (24), respectively. Table II lists the control parameters along with the results of the experimental study introduced below.

B. Simulation Results

For the system shown in Fig. 1, simulation work is carried out in the PSIM environment using the parameters listed in Table I. Discrete models for the active damper and the PR controller are constructed using PSIM digital control modules. Unipolar PWM is adopted for the inverter. To verify the proposed approach, step changes in the reference current are carried out twice (from a half to the rated current and back). Figs. 17, 18 and 19 show simulation waveforms of the grid voltage and grid current using the designed parameters listed in Table II at the different resonant frequencies.

C. Experimental Results

A prototype single phase inverter was connected, using an *LCL* filter, to an AC source for grid emulation. The control

TABLE I
SYSTEM PARAMETERS

Symbol	Quantity	Value
P	Rated power	1 kw
V_g	Grid voltage	120 V
F_o	Grid Frequency	50 Hz
V_{dc}	DC Voltage	220 V
L_i	Inverter side inductance	2.75 mH
L_g	Grid side inductance	1.2 mH
C	Capacitance	22.2 µF, 12.2 µF, 5.4 µF, and 3.3 µF
F_{sw}	Switching Frequency	8 kHz
F_s	Sampling Frequency	8 kHz

scheme was implemented using a C6713-A DSP development board. A step change in the reference current was carried out to verify the transient characteristics. Experimental investigations have been conducted using the parameters listed in Table II at different resonant frequencies.

For ω_{res1} ($< \omega_s/6$), an active damper (AD) is mandatory to maintain stability. This is confirmed by Fig. 20(a) where a high oscillatory current is produced without using AD. On the other hand, when using AD, Fig. 20(b) shows that the stability is restored. These waveforms indicate clearly the stabilization effect of the active damping loop for resonant frequencies of less than one-sixth of the control frequency.

For resonant frequencies greater than one-sixth of the control frequency, AD is not mandatory for system stability. However, the stability can be worse with variations in grid side inductance. Moreover, oscillatory resonant currents can be generated without using resonance damping. This is confirmed in Fig. 21(a), where the current waveforms at ω_{res2} are shown without using AD. In this case, oscillatory resonant currents are generated at the stepping up of the reference current. Much worse oscillations can be generated if the grid voltage contains harmonic components around the resonant frequency. On the other hand, the waveforms when using AD are shown Fig. 21(b). It can be realized that the mitigation effect is introduced by the AD in this case. Finally, Figs. 22(a) and 22(b) show the waveforms when using AD for ω_{res3} and ω_{res4}, respectively.

At steady state conditions, Table II presents the measured

TABLE II
DESIGNED PARAMETERS AND EXPERIMENTAL RESULTS

C (μF)	β_{res}	Designed Controller				Experimental Results		
		β_h	r	K_p	K_r	I_{g1}	E_{ss}	PF
22.2	0.146	0.4	0.24	6.84	1678	8	0.04	0.999
12.2	0.197	0.4	0.16	8.41	1854	8.01	0.039	0.999
5.4	0.296	0.25	-0.1	14.01	2427	7.98	0.042	0.999
3.3	0.379	0.25	-0.18	15.56	2600	8.03	0.037	0.999

TABLE III
THD OF THE CURRENT WAVEFORMS

C (μF)	βres	Without AD	With AD
22.2	0.146	–	3.32%
12.2	0.197	3.02 %	3.09%
5.4	0.296	–	2.27%
3.3	0.379	–	2.7%

fundamental current component (I_{g1}), the power factor (PF), and the steady state error $\left(E_{ss} = \left|(I_{ref} - I_{g1})/I_{ref}\right| \times 100\right)$. These results reflect satisfactory transient and steady state behavior along with resonance damping over the entire possible range of resonant frequencies.

The total harmonic distortion of the measured grid current (THD$_i$) has been estimated at the rated conditions as ratio (in %) of the harmonic current (of the orders 2 to 40) to the fundamental current as listed in table III. For values of the resonant frequencies, it is shown that THD$_i$ is less than 5%. For ω_{res2}, it is shown that adding the AD loop increases the THD$_i$ value from 3.02% to 3.09%. This indicates the negligible effect of the AD loop on the THD$_i$ of the grid current.

VII. CONCLUSIONS

This paper investigates active damping of *LCL* filter resonance using HPF of the grid current feedback. A new expression for this HPF, in terms of the filter components, has been derived. This expression facilitates a general stability study of the active damped filter. Through discrete time domain investigation of the active damped filter, three regions of resonant frequencies have been identified for stable open loop behavior at a certain HPF cutoff frequency. These regions cover a wide range of resonant frequencies up to 0.45 of the sampling frequency. Moreover, straightforward design steps for both the HPF and the fundamental current regulator have been proposed. A numerical example and experimental work have been introduced. The results show that good steady state and dynamic performance along with resonance damping can be obtained over a wide range of resonant frequencies using the proposed co-design steps of the control parameters.

REFERENCES

[1] W. Weimin, Y. Liu, Y. He, H. S. Chung, M. Liserre, and F. Blaabjerg, "Damping methods for resonances caused by LCL-filter-based current-controlled grid-tied power inverters: An overview." *IEEE Trans. Ind. Electron.*, Vol. 64, No. 9, pp 7402-74013 Sep. 2017.

[2] J. Sampath and M. Hanif, "Generalized LCL-filter design algorithm for grid-connected voltage-source inverter," *IEEE Trans. Ind. Electron.*, Vol. 64, No. 3, pp 1905-1915, Mar. 2017.

[3] H. Komurcugil, S. Bayhan, and H. Abu-Rub, "Variable- and fixed-switching-frequency-based HCC methods for grid-connected VSI With active damping and zero steady-state error," *IEEE Trans. Ind. Electron.*, Vol. 64, No. 9, pp. 7009-7018, Sep. 2017.

[4] F. Wu, B. Sun, K. Zhao, and L. Sun, "Analysis and solution of current zero-crossing distortion with unipolar hysteresis current control in grid-connected inverter," *IEEE Trans. Ind. Electron.*, Vol. 60, No. 10, pp. 4450-4457, Oct. 2013.

[5] F. Wu, L. Zhang, and Q. Wu, "Simple unipolar maximum switching frequency limited hysteresis current control for grid-connected inverter," *IET Power Electron.*, Vol. 7, No. 4, pp. 933-945, Apr. 2014.

[6] F. Wu, X. Li, and J. Duan, "Improved elimination scheme of current zero-crossing distortion in unipolar hysteresis current controlled grid-connected inverter," *IEEE Trans. Ind. Inform.*, Vol. 11, No. 5, pp. 1111-1118, Oct. 2015.

[7] F. Wu, F. Feng, L. Luo, J. Duan, and L. Sun, "Sampling period online adjusting-based hysteresis current control without band with constant switching frequency," *IEEE Trans. Ind. Electron.*, Vol. 62, No. 1, pp. 270-277, Jan. 2015.

[8] X. Hao, X. Yang, T. Liu, L. Huang, and W. Chen, "A sliding-mode controller with multiresonant sliding surface for single-phase grid-connected VSI with an LCL filter," *IEEE Trans. Power Electron.*, Vol. 28, No. 5, pp. 2259-2268, May 2013.

[9] H. Komurcugil, S. Ozdemir, I. Sefa, N. Altin, and O. Kukrer, "Sliding-mode control for single-phase grid-connected LCL-filtered VSI with double-band hysteresis scheme," *IEEE Trans. Ind. Electron.*, Vol. 63, No. 2, pp. 864-873, Feb. 2016.

[10] S. Eren, M. Pahlevaninezhad, A. Bakhshai, and P. K. Jain, "Composite nonlinear feedback control and stability analysis of a grid-connected voltage source inverter with LCL filter," *IEEE Trans. Ind. Electron.*, Vol. 60, No. 11, pp. 5059-5074, Nov. 2013

[11] H. Komurcugil, N. Altin, S. Ozdemir, and I. Sefa, "Lyapunov-function and proportional-resonant-based control strategy for single-phase grid-connected VSI with LCL filter," *IEEE Trans. Ind. Electron.*, Vol. 63, No. 5, pp. 2838-2849, May 2016.

[12] D. Chen, J. Zhang, and Z. Qian, "An improved repetitive control scheme for grid-connected inverter with frequency-adaptive capability," *IEEE Trans. Ind. Electron.*, Vol. 60, No. 2, pp. 814-823, Feb. 2013.

[13] J. Rodriguez, J. Pontt, C. A. Silva, P. Correa, P. Lezana, P. Cortes, and U. Ammann, "Predictive current control of a voltage source inverter," *IEEE Trans. Ind. Electron.*, Vol. 54, No. 1, pp. 495-503, Feb. 2007.

[14] A. Bouafia, F. Krim, and J.-P. Gaubert, "Fuzzy-logic-based switching state selection for direct power control of three-phase PWM rectifier," *IEEE Trans. Ind. Electron.*, Vol. 56, No. 6, pp. 1984-1992, Jun. 2009.

[15] X. Fu and S. Li, "Control of single-phase grid-connected converters with LCL filters using recurrent neural network and conventional control methods," *IEEE Trans. Power Electron.*, Vol. 31, No. 7, pp. 5354-5364, Jul. 2015.

[16] J. Dannehl, C. Wessels, and F. W. Fuchs, "Limitations of voltage-oriented pi current control of grid-connected PWM rectifiers with LCL filters," *IEEE Trans. Ind. Electron.*, Vol. 56, No. 2, pp. 380-388, Feb. 2009.

[17] G. Shen, X. Zhu, J. Zhang, and D. Xu, "A new feedback method for PR current control of lcl-filter-based grid-connected inverter," *IEEE Trans. Ind. Electron.*, Vol. 57, No. 6, pp. 2033-2041, Jun. 2010.

[18] M. Castilla, J. Miret, J. Matas, L. Garcia de Vicuna, and J. M. Guerrero, "Control design guidelines for single-phase grid-connected photovoltaic inverters with damped resonant harmonic compensators," *IEEE Trans. Ind. Electron.*, Vol. 56, No. 11, pp. 4492-4501, Nov. 2009.

[19] B. Bahrani, M. Vasiladiotis and A. Rufer, "High-order vector control of grid-connected voltage-source converters with LCL-filters," *IEEE Trans. Ind. Electron.*, Vol. 61, No. 6, pp. 2767-2775, Jun. 2014.

[20] J. Dannehl, M. Liserre, and F. W. Fuchs, "Filter-based active damping of voltage source converters with LCL filter," *IEEE Trans. Ind. Electron.*, Vol. 58, No. 8, pp. 3623-3633, Aug. 2011.

[21] B. S. Romdhane, M. Naouar, I. B.elkhodja, and E. Monmasson, "Robust active damping methods for LCL filter-based grid-connected converters," *IEEE Trans. Power Electron.*, Vol. 32, No. 9, pp 6739-6750, Sep. 2017.

[22] D. Pan, X. Ruan, C. Bao, W. Li, and X. Wang, "Capacitor-current-feedback active damping with reduced computation delay for improving robustness of LCL-type grid-connected inverter," *IEEE Trans. Power Electron.*, Vol. 29, No. 7, pp. 3414-3427, Jul. 2014.

[23] A. Aapro, T. Messo, T. Roinila, and T. Suntio, "Effect of active damping on output impedance of three-phase grid-connected converter," *IEEE Trans. Ind. Electron.*, Vol. 64, No. 9, pp. 7532-7541, Sep. 2017

[24] R. P-Alzola, M. Liserre, F. Blaabjerg, R. Sebastián, J. Dannehl, and F. W. Fuchs, "Systematic design of the lead-lag network method for active damping in LCL-filter based three phase converters," *IEEE Trans. Ind. Inform.*, Vol. 10, No. 1, pp. 43-52, Feb. 2014.

[25] X.Wang, F. Blaabjerg, and P. C. Loh, "Virtual RC damping of LCL-filtered voltage source converters with extended selective harmonic compensation," *IEEE Trans. Power Electron.*, Vol. 30, No. 9, pp. 4726-4737, Sep. 2015.

[26] B. Wang, Y. Xu, Z. Shen, J. Zou, C. Li, and H. Liu, "Current control of grid-connected inverter with LCL filter based on extended-state observer estimations using single sensor and achieving improved robust observation dynamics," *IEEE Trans. Ind. Electron.*, Vol. 64, No. 7, pp. 5428-5439, Jul. 2017.

[27] C. A. Busada, S. G. Jorge, and J. A. Solsona, "Full-state feedback equivalent controller for active damping in LCL filtered grid connected inverters using a reduced number of sensors," *IEEE Trans Ind. Electron.*, Vol. 62, No. 10, pp.

5993-6002, Oct. 2015.

[28] J. Kukkola, M. Hinkkanen, and K. Zenger, "Observer-based state-space current controller for a grid converter equipped with an LCL filter: Analytical method for direct discrete-time design," *IEEE Trans Ind. Appl.*, Vol. 51, No. 5, pp. 4079-4090, Sep./Oct. 2015.

[29] R. Guzman, L. G. de Vicuna, J. Morales, M. Castilla, and J. Miret, "Model-based active damping control for three-phase voltage source inverters with LCL filter," *IEEE Trans. Power Electron.*, Vol. 32, No. 7, pp. 5637-5650, Jul. 2017

[30] L. Harnefors, A. G. Yepes, A. Vidal, and J. Doval-Gandoy, "Passivity-based controller design of grid-connected VSCs for prevention of electrical resonance instability," *IEEE Trans. Ind. Electron.*, Vol. 62, No. 2, pp. 702-710, Feb. 2015.

[31] X. Li, X. Wu, Y. Geng, X. Yuan, C. Xia, and X. Zhang, "Wide damping region for LCL-type grid-connected inverter with an improved capacitor-current-feedback method," *IEEE Trans. Power Electron.*, Vol. 30, No. 9, pp. 5247-5259, Sep. 2015.

[32] J. Xu, S. Xie, and T. Tang, "Active damping-based control for grid-connected LCL-filtered inverter with injected grid current feedback only," *IEEE Trans. Ind. Electron.*, Vol. 61, No. 9, pp. 4746-4758, Sep. 2014.

[33] C. Dick, S. Richter, M. Rosekeit, J. Rolink, and R. De Doncker, "Active damping of LCL resonance with minimum sensor effort by means of a digital infinite impulse response filter," in *Proc. EPE 2007*, pp. 1-8, 2007.

[34] M. Hanif, V. Khadkikar, W. Xiao, and J. L. Kirtley, "Two degrees of freedom active damping technique for LCL filter-based grid connected PV systems," *IEEE Trans. Ind. Electron.*, Vol. 61, No. 6, pp. 2795-2803, Jun. 2014.

[35] X. Wang, F. Blaabjerg, and P. Chiang Loh, "Grid-current-feedback active damping for LCL resonance in grid-connected voltage source converters," *IEEE Trans. Power Electron.*, Vol. 31, No. 1, pp. 213-223, Jan. 2016.

[36] M. A. Gaafar, G. M. Dousoky, E. M. Ahmed, M. Shoyama, "Systematic design of grid-current-based active damping for grid-connected LCL filters," *2017 IEEE Applied Power Electronics Conference and Exposition (APEC)*, 2017.

[37] G. F. Franklin, J. D. Powell, and M. L Workman, *Digital Control of Dynamic Systems*, 2nd ed., California: Addison Wesley Longman, Inc., p. 461, 1998.

Mahmoud A. Gaafar received his B.Sc. and M.Sc. degrees in Electrical Engineering from Aswan University, Aswan, Egypt, in 2004 and 2010, respectively. He received his Ph.D. degree from the Department of Electrical and Electronic Engineering, Graduate School of Information Science and Electrical Engineering, Kyushu University, Fukuoka, Japan, in 2017. He is presently working as an Assistant Professor in the Department of Electrical Engineering, Aswan University. He is a Member of the Aswan Power Electronics Application Research Center (APEARC), Aswan University. His current research interests include harmonics mitigation, grid-connected converters and digital control strategies. He is a Member of the IEEE Power Electronics Society (PELS).

Gamal M. Dousoky was born in Minia, Egypt, in 1977. He received his B.Sc. and M.Sc. degrees from Minia University, Egypt, in 2000 and 2004, respectively, and his PhD in 2010 from Kyushu University, Japan (all in Electrical and Electronic Engineering). Since 2000 he has been associated with the Dept. of Elect. Eng., Faculty of Eng., Minia University, in March 2017 he was promoted to the position of an Associate Professor position. He worked as Postdoctoral research fellow at Kyushu University for two years. His research interests include power electronics, particularly renewable-energy applications, energy efficiency, switching power supplies, electromagnetic interference/compatibility, and digital control. He authored and co-authored more than 70 publications, in international journals and conference proceedings of Power Electronics and Industrial Technologies. Dr. Gamal received the 2009 Excellent Student Award of the IEEE Fukuoka Section. He is an IEEE Senior member, and a reviewer in many international journals and conferences.

Emad M. Ahmed received his B.Sc. and M.Sc. degrees from the Dept. of Electrical Engineering, Aswan University, EGYPT in 2001, 2006, respectively. In addition, he received the Ph.D. degree from the Dept. of Electrical Engineering, Kyushu University, JAPAN in 2012. Currently, he is an associate Professor with the Dept. of electrical engineering, Aswan University, Egypt. His present research interests include applied power electronics especially in renewable energy applications, Micro-grids, and Fault Tolerant control. He has incorporated in several research projects in power electronic and renewable energy applications. Dr. Emad received Baek-Hyun Award from the Korean Institute of Power Electronics (KIPE) for his academic contribution in the field of power electronics in 2012. He is a member in IEEE Power Electronics Society (PELS), IEEE Industrial Electronics Society (IES), and IEEE Industrial Application Society.

Masahito Shoyama received his B.S. degree in Electrical Engineering and his Ph.D. degree from Kyushu University, Fukuoka, Japan, in 1981 and 1986, respectively. He joined the Department of Electronics, Kyushu University as a Research Associate, in 1986. He became an Associate Professor in 1990, and he has been a Professor since 2010. Since 2009, he has been with the Department of Electrical Engineering, Faculty of Information Science and Electrical Engineering, Kyushu University. He has been active in the field of power electronics, especially in the areas of bi-directional converters for DC/AC power systems, high-frequency switching converters for renewable energy sources, power factor correction (PFC) converters, and electromagnetic compatibility (EMC). Professor Shoyama is a Member of the IEEE, IEICE, IEEJ and SICE.

Mohamed Orabi received his Ph.D. degree from Kyushu University, Fukuoka, Japan, in 2004. He is presently working as a Professor at Aswan University, Aswan, Egypt. He is the Founder and Director of the Aswan Power Electronics Application Research Center (APEARC), Aswan University. In addition, he was with Enpirion Inc. and Altera Corp., where was the Senior Manager of the Altera-Egypt Technology Center, from June 2011 to July 2014. He has published about 200 papers in international journals and conference proceedings. His current research interest includes dc-dc and PFC converters, integrated power management, nonlinear circuits and inverter designs for renewable energy applications. He has lead several projects related to power electronics applications for renewable energy. Professor Orabi is an Associate Editor of the IET Power Electronics Journal and a Guest Editor of the IEEE JESTPE. He is also the Chair of the PELS Egypt Chapter. Dr. Orabi was a recipient of a 2002 Excellent Student Award of the IEEE Fukuoka Section and a Best Young Research Award from the IEICE Society, Japan, in 2004. He also received a SVU Encouragement Award in 2009, a National Encouragement Award in 2010, and Aswan University Supervision Awards for 2015 and 2016.